Relighting Scenes with Object Insertions in Neural Radiance Fields

Xuening Zhu,* Renjiao Yi,* Xin Wen, Chenyang Zhu, Kai Xu†
National University of Defense Technology

Figure 1. We propose a method for inserting object NeRFs into scene NeRFs. From left to right, the figure depicts input images, object insertion without relighting, and relightings from novel views. The method also supports non-Lambertian relighting and material rendering, as the pillow on the chair.

Abstract

The insertion of objects into a scene and relighting are commonly utilized applications in augmented reality (AR). Previous methods focused on inserting virtual objects using CAD models or real objects from single-view images, resulting in highly limited AR application scenarios. We propose a novel NeRF-based pipeline for inserting object NeRFs into scene NeRFs, enabling novel view synthesis and realistic relighting, supporting physical interactions like casting shadows onto each other, from two sets of images depicting the object and scene. The lighting environment is in a hybrid representation of Spherical Harmonics and Spherical Gaussians, representing both high- and low-frequency lighting components very well, and supporting non-Lambertian surfaces. Specifically, we leverage the benefits of volume rendering and introduce an innovative approach for efficient shadow rendering by comparing the depth maps between the camera view and the light source view and generating vivid soft shadows. The proposed method achieves realistic relighting effects in extensive experimental evaluations.

1. Introduction

Object insertion is widely used across various industries, such as augmented reality (AR), virtual reality (VR), and the animation and film sectors. The goal of object inser-tion is to seamlessly integrate objects into scenes, enhancing visual immersion for users. Traditional computer graphics methods typically involve manually capturing and reconstructing the physical world, encompassing geometry, texture, and other attributes. The conventional industrial process often involves manually composing CAD models of scenes and objects, and using traditional rendering techniques like rasterization and ray tracing for relighting or generating new views, to create a customized visual experience. Nonetheless, this process is labor-intensive and not user-friendly for beginners.

In this paper, we aim to introduce a thorough pipeline for compositing and relighting 3D objects and scenes solely based on image inputs. Addressing this challenge encompasses various highly ambiguous tasks, including 3D reconstruction, inverse rendering, and image-based rendering. NeRF [30] provides a method that connects images and 3D scenes by utilizing MLPs and volume rendering to achieve realistic, high-quality effects in a straightforward manner. Therefore, we incorporate NeRF as the backbone of our proposed pipeline for end-to-end differentiable reconstruction and relighting.

One drawback of NeRF is its inherent coupling of geometry, illumination, and material information within its representation. This interconnectedness presents challenges when trying to directly employ NeRFs for composing and editing 3D objects and scenes. Other challenges in applying NeRF for relighting include: Firstly, NeRF simplifies vol-

ume rendering by assuming that particles are self-luminous, the light of particle radiation couples the light and material properties. Furthermore, the ambient light in the input image remains undetermined, impeding support for lighting editing. Secondly, there is a lack of a lighting rendering pipeline that accommodates both low- and high-frequency lighting sources, and supports spatially-variant lighting and non-Lambertian surfaces in NeRFs. Lastly, NeRF treats shadows as part of the color of objects, disregarding the visibility of incoming light sources, thus limiting its ability to produce realistic shadow effects.

To address the first challenge, we propose decoupling NeRF outputs into illumination-related and material-related terms, i.e. decomposing the color into reflectance and shading components. This approach effectively resolves the intrinsic decomposition of NeRFs in a completely unsupervised manner. With decomposed geometry, material, and lighting, we can further edit the scene by inserting object NeRFs into scene NeRFs and fitting them into the scene illumination by the proposed shading replacement, or relighting the whole composited scene.

Addressing the second challenge, many differentiable lighting rendering methods, such as Pytorch3D, utilize point lights. However, employing a large number of point lights for an environment map can be computationally intensive, particularly for low-frequency lighting. To overcome this, we introduce a hybrid lighting representation by combining Spherical Harmonics and Spherical Gaussians to respectively represent low- and high-frequency components. Leveraging rendering layers from [65], our approach enables the rendering of non-Lambertian surfaces and the editing of materials for each point. Spherical Gaussians are used to fill the gap between Spherical Harmonics lighting and original HDR environment maps. Furthermore, in our pipeline, except distant lighting as many prior works, we can also put Spherical Gaussian lighting at 3D positions, supporting spatially-variant lighting.

Regarding the third challenge, previous studies have proposed two approaches for modeling light source visibility. One approach involves directly predicting the visibility of light sources for each point through neural networks but is limited to static scenes where scene geometry remains constant. The alternative approach generates shadow rays from each 3D point to the light source, using the density of sampling points on the shadow ray as the light source visibility coefficient for the 3D point. While this method is more suitable for composited or edited scenes, the extensive computation required to generate shadow rays significantly slows down shadow rendering. In response, we introduce the variance shadow mapping strategy into volume rendering by comparing the depths from the light source's perspective, and Chebyshev's inequality to generate soft shadows. This innovative approach delivers comparable results to conventional methods while substantially enhancing efficiency in both time and computation resources.

The whole pipeline is end-to-end and differentiable, in an unsupervised manner. The contributions are summarized as follows:

- We propose a method to insert object NeRF into scene NeRF while fitting into the scene illumination, by solving the intrinsic decomposition of NeRFs unsupervisedly.

- We propose a pipeline to relight the composited scene, with a hybrid lighting representation of Spherical Harmonics and Spherical Gaussians, supporting non-Lambertian surfaces, cast shadows, and spatially variant light sources.

- We introduce an efficient way of variance shadow mapping in NeRFs, for realistic soft shadow rendering.

2. Related Works

2.1. Inverse Rendering

Before NeRFs, methods [64, 66] of object insertion usually insert virtual objects into the image, not supporting renderings from novel views. With inverse rendering, methods can re-render real objects from images into another scene [65]. The goal of inverse rendering is to extract the geometry, material properties, and lighting information of a scene from image inputs, for further manipulations such as relighting or material editing. Classical methods typically depend on optical devices to measure various physical factors, including geometric structures. Neural networks have recently emerged as a solution for tasks like scene relighting and inverse rendering. The representative CGIntrinsic [23] decomposes the reflectance and grayscale shading of the scene by learning and realizes approximate lighting editing by modifying Shading. However, it is limited to altering the lighting of static images and does not facilitate the generation of new perspective views of the modified scene. NeRF [30] achieves high-quality new perspective synthesis effects by representing scenes with implicit MLP, and a large number of related improvements [4, 11, 24, 31, 36, 63] have emerged since then. Some NeRF-based methods [6–9, 12, 19, 39, 42, 60, 70, 71, 73], model the BRDF, illumination intensity, and illumination visibility separately to achieve inverse rendering. Since directly decomposing these attributes from a single static scene is an ill-posed problem, prior knowledge, such as known illumination or input images depicting different lighting scenarios, is commonly incorporated.

Zeng *et al.* [69] introduce a relightable radiance field that utilizes known light sources as inputs to achieve accurate highlights and shadows. Lyu *et al.* [29] follow the
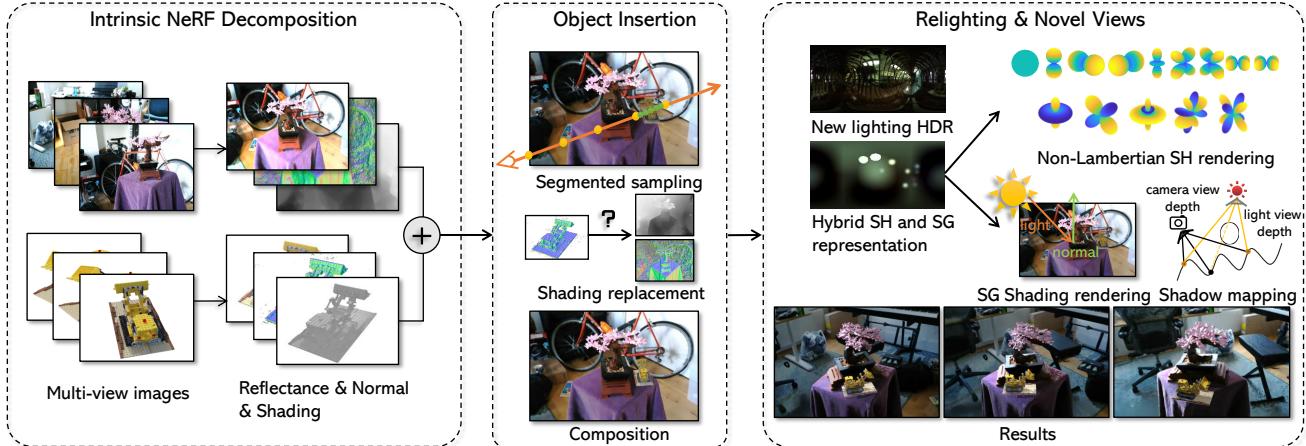
Figure 2. Overview of the method. Given two sets of multi-view images of a scene and an object from unknown lighting environments, our method reconstructs and predicts the intrinsic decomposition of the scene and object. Subsequently, it composites their geometry through segmented sampling, updating the object's shading to match the scene illumination. At last, non-Lambertian relighting of the composited scene is proposed with the hybrid lighting representation and efficient shadow mapping.

idea of PRT to represent the transmission results of lighting and use Mitsuba to add OLAT images as supervision for inverse rendering. IntrinsicNeRF [62] achieves intrinsic image decomposition in NeRFs. These papers focus on the inverse rendering process and relighting of the scene, without changing the scene by adding or deleting objects. Our paper focuses on the composition of scene and object, where inverse rendering is adopted to support the relighting of NeRF, for realistic composition and AR results. It supports spatially variant light sources and cast shadow rendering in relighting.

2.2. Scene Composition in NeRFs

Related methods [18, 21, 22, 44, 48, 51, 57–59] can be roughly divided into the composition of inputs of MLPs and the composition of color and voxel density. Control-NeRF [22] is a typical method for compositing inputs, they propose to separate the scene representation and the network to learn a potential scene feature representation. This method improves the generalization of NeRF and can quickly achieve scene composition, but it does not consider the impact of illumination. Yang *et al*. [59] propose two MLP branches to model the background and object properties respectively to separate individual objects from the scene. Sosuke *et al*. [21] adopt one branch for predicting the color of voxels and the other branch to predict semantic features, separating individual objects by semantic separation. Tang *et al*. [44] learn a hybrid tensor rank decomposition of the scene, which can be arbitrarily composited into one scene by concatenating along the rank dimension. These methods focus more on how to separate individual objects from complex scenes. They edit objects that are

originally from the scene, where they do not have to consider the consistency of illumination and often ignore the rationality of post-composition shadows. Different from these methods, the goal of our paper is to realize object insertion into scenes, fitting into the scene illumination, and support further relighting.

2.3. Shadow Mapping

Shadow mapping is a conventional technique for rendering shadows in computer graphics, and the advancement of technology has led to the development of numerous shadow mapping algorithms. Initially, shadow mapping [55] compares the depth of the light source view to determine the presence of shadows, resulting in distinct hard shadows. To address the issue of soft shadows, many methods have been developed [1, 14, 15, 32, 37]. The Percentage-Closer soft shadow [37] method incorporates multiple depths and blends them to generate soft shadows. The variance shadow mapping method [14] utilizes depth variance to achieve soft shading effects through the application of Chebyshev inequality. Additionally, some approaches utilize neural networks for fractional shadow calculations, as demonstrated by references such as Karnieli *et al*. and others [2, 45]. These methods employ neural networks to learn depth and generate shadows, often represented as scenes produced through supervised learning techniques. In this paper, we introduce Variance Shadow Mapping (VSM) into Neural Radiance Fields (NeRF) for end-to-end relighting.

3. Method

As presented in Fig. 2, given two sets of posed images of a scene and an object, $\{I_{si}, C_{si}\}_{i=1}^{N_s}$ and $\{I_{oi}, C_{oi}\}_{i=1}^{N_o}$, both

captured in an unknown lighting environment. I is the RGB image and C is the camera pose. We aim to insert the object into the scene. The method includes three parts. The first part is to how to obtain the intrinsic NeRFs, which is introduced in Section 3.1. The second part is the object insertion into the scene, which is introduced in Section 3.2. The third part is relighting of the composited scene, as introduced in Section 3.3.

3.1. Intrinsic NeRF Decomposition

3.1.1 Intrinsic NeRF Model

To address the highly ill-posed problem of inverse rendering 3D scenes without any supervision, we utilize a simplified model known as intrinsic image decomposition. Our model has three outputs: density σ, reflectance $\mathbf{R} \in R^3$ and shading $\mathbf{S} \in R$, i.e. $F_I(X, D) = (\sigma, \mathbf{R}, \mathbf{S})$. While reflectance is solely dependent on the object's properties, we only use the 3D locations as input for the reflectance MLP. On the other hand, shading is influenced by the location and viewing perspective. Therefore, the inputs for the shading MLP include the location and view direction. Without any additional input, we only use the RGB images for supervision:

$$
\begin{aligned}
\hat{\mathbf{C}}(\mathbf{r}) &= \int_{t_n}^{t_f} T(t)\sigma(t)\big(\mathbf{S}(t) \cdot \mathbf{R}(t)\big)dt, \\
\mathcal{L} &= \frac{1}{|\mathcal{R}|} \sum_{\mathbf{r} \in \mathcal{R}} \|\hat{\mathbf{C}}(\mathbf{r}) - \mathbf{C}(\mathbf{r})\|_2^2,
\end{aligned}
\tag{1}
$$

where $\mathbf{C}(\mathbf{r})$ is the ground truth RGB, $\mathcal{R}$ denotes the set of camera rays in a single batch.

3.1.2 Decomposition of Geometry

Given an arbitrary view and the intrinsic neural radiance field, normal and depth maps of the view can be computed easily:

$$
\begin{aligned}
\mathbf{D}(\mathbf{r}) &= \int_{t_n}^{t_f} T(t)\sigma(t)t\,dt, \\
\mathbf{N}(\mathbf{r}) &= \int_{t_n}^{t_f} T(t)\sigma(t)\big(-\nabla(\sigma)\big)dt.
\end{aligned}
\tag{2}
$$

To enhance the precision and smoothness of geometry for improved subsequent rendering tasks, we introduce a regularization term for normal directions to ensure consistency among adjacent points. Following the pinhole camera model, a pixel in the background corresponds to a larger physical area. To guide the regularization process, we introduce a depth-dependent weight represented as:

$$
\mathcal{L}_d = \frac{1}{|\mathcal{R}|} \sum_{\mathbf{r} \in \mathcal{R}} \Big(1 - \frac{\mathbf{N}(\mathbf{r}) \cdot \mathbf{N}(\mathbf{r}_{adj})}{|\mathbf{N}(\mathbf{r})||\mathbf{N}(\mathbf{r}_{adj})|}\Big)\frac{1}{\mathbf{D}(\mathbf{r})^2}, \tag{3}
$$

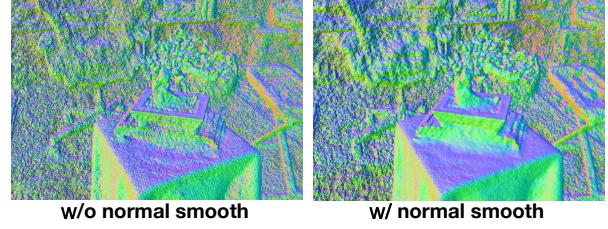**w/o normal smooth**　　**w/ normal smooth**

Figure 3. Visualizations comparing cases with (on the right) and without (on the left) the term $\mathcal{L}_d$. This row displays illustrative examples from a scene.

where $\mathbf{N}(\mathbf{r})$ is the normal of pixel $\mathbf{r}$, $\mathbf{N}(\mathbf{r}_{adj})$ is the normal of the neighborhood around pixel $\mathbf{r}$. The comparison is shown in Fig. 3. It is evident that the normal maps in the first column (without smoothness regularization) exhibit significantly more noise, whereas the normal maps in the second column with smoothness regularization appear smoother. This regularization is crucial, particularly for complex scenes.

3.1.3 Decomposition of Reflectance and Shading

Reflectance is an inherent attribute of surfaces and represents the material properties of objects and scenes, independent of illumination. In traditional intrinsic image decomposition, constraints of reflectance chromaticities $\mathcal{L}_{chro}$, sparsity $\mathcal{L}_{rs}$ and non-local sparsity $\mathcal{L}_{nrs}$ are commonly used for optimization. Here we introduce similar priors into the NeRF-based backbone.

Additionally, a scale ambiguity exists between shading and reflectance in intrinsic image decomposition, where scaling factors of k on reflectance and 1/k on shading do not impact the observed image. To overcome unreasonable brightness changes in the reflectance, we constrain the consistency of reflectance and brightness of different points. It ensures that the shading of new objects matches the brightness level of the scene shading when inserted into the scene, avoiding excessive brightness or darkness. Specifically, a mean reflectance regularization is used to constrain the reflectance of different scenes at the same level:

$$
\mathcal{L}_{mean\_r} = \frac{1}{|\mathcal{R}|} \sum_{\mathbf{r} \in \mathcal{R}} \Big|\big(\mathbf{R}(\mathbf{r}).max\big) - \beta_{avg\_r}\Big|, \tag{4}
$$

where β_{avg_r} is a hyperparameter, and it is set as 0.6 for most scenes. $\mathbf{R}(\mathbf{r}).max$ represents the highest value of reflectance in the RGB channels.

Shading represents the brightness of the light reflected from one point to the viewpoint and conveys information about environmental illumination. The shading smoothness $\mathcal{L}_s$ is defined as the variance of shading for all the pixels in a single batch. Since shading and surface normal are correlated, there exists a consistency between shading and nor-

w/o segmented sampling   **w/ segmented sampling**

Figure 4. Visualization of the rendered images depicting the segmented sampling strategy. Part of the Lego is missing on the left image.

mal:

$$\mathcal{L}_{sn} = \frac{1}{|\mathcal{R}|} \sum_{\mathbf{r} \in \mathcal{R}} \omega_n(\mathbf{r}, \mathbf{r}') * |\mathbf{S}(\mathbf{r}) - \mathbf{S}(\mathbf{r}')| * (1 - tanh(\mathbf{Dis}(\mathbf{r}, \mathbf{r}')),$$

(5)

where ω_n measures the cosine similarity of $\mathbf{r}$ and $\mathbf{r}'$, $\mathbf{Dis}(\mathbf{r}, \mathbf{r}')$ represents the distance between their respective 3D points.

The intrinsic NeRF decomposition is trained by summing all the losses:

$$\begin{aligned} \mathcal{L}_{train} =& \lambda_0 \mathcal{L} + \lambda_1 \mathcal{L}_d + \lambda_2 \mathcal{L}_{mean\_r} + \lambda_3 \mathcal{L}_{chro} \\ &+ \lambda_4 \mathcal{L}_{rs} + \lambda_5 \mathcal{L}_{nrs} + \lambda_6 \mathcal{L}_s + \lambda_7 \mathcal{L}_{sn}, \end{aligned}$$

(6)

where all the λ are adjustable weights.

3.2. The Composition of Scene and Object

Once the intrinsic NeRFs of the scene and the object are obtained respectively, we can insert objects into scenes based on geometry and shading. This composited scene can then be rendered from different views for new view synthesis, similar to the original NeRF approach.

3.2.1 Geometry Composition by Segmented Sampling

Given the inserting position and orientation in the scene (i.e. the translation and rotation between the coordinate systems of the object and scene), sampling points in the scene can be transformed to obtain the point coordinates in the object's coordinate system. The σ-density, reflectance, and shading of the corresponding points are composited separately. The composited density is the normalized sum of densities of corresponding points from the scene and the object at the same position. The reflectance is the weighted sum of reflectance values of corresponding points, where the weights are the densities of the voxel particles. Shading can be composited similarly if not considering relighting. The final image can be rendered following Eqn. 1.

However, during the experiment, it was observed that direct composition could lead to missing areas of the object in the rendered images, as shown in Fig. 4. This issue arises due to insufficient sampling in the object area. Since scenes are typically larger than objects, the distance between adjacent sampling points in the scene is uniform. The sampling points on the object may be sparse because the object NeRF's size is smaller than the scene. As shown in Fig. 4 (left), when sampling points are sparse on the object, it is possible that some parts of the object fall between two sampled points, and completely missing in the rendered images. It will lead to inaccurate probability density distribution (PDF) in the fine stage of sampling of NeRFs. This problem is very common in experiments. To solve the problem, a new sampling strategy called segmented sampling is proposed. This method selectively increases the sampling rate only within the bounding box of the object area to ensure detailed sampling without significantly increasing the overall number of sampling points and computational cost. This segmented sampling approach aims to capture the object details accurately while maintaining efficiency in the rendering process.

3.2.2 Relighting the Object into Scene Illumination

The illumination of different scenes and objects usually varies greatly, and a naive composition without considering lighting consistency would lead to unrealistic results. It is crucial to update the shading to ensure a realistic integration. However, as the scene illumination is unknown, re-rendering shading from scratch is not feasible. We propose a shading replacement method to quickly generate object shading under the scene's illumination. For Lambertian scenes, points with similar surface normals tend to have similar shading. Therefore, we can replace the shading of each object point with the shading of a nearby scene point that shares a similar normal vector. By finding these matching pairs and averaging their shading values, we can simulate the object shading under the scene illumination without direct knowledge of the lighting conditions. Specifically, for each object point, we can find scene points of similar normal vectors to form a pair. Since many scene points are similar in normal, there are many pairs for an object point. These pairs are ranked according to the normal similarities and distances between the object point and the scene points, and the mean shading value of the top-ranked ones $\mathbf{S}_{mean}$ is taken as the re-rendered shading value of the object point. In addition, the resulting shading needs to complement the difference in reflectance brightness by $\mathbf{S}_{updated} = \mathbf{S}_{mean} \frac{\beta^s_{avg\_r}}{\beta^o_{avg\_r}}$, $\beta^s_{avg\_r}$ and $\beta^o_{avg\_r}$ are the average brightness of reflectance of the scene and the objects respectively. Fig. 13 shows that by this way, inserting object around the edge between a bright and a dark region gives a reasonable shading.

3.3. Relighting the Composited Scene

In this section, we introduce how to render the composited scene under new HDR lighting.

3.3.1 Hybrid Parametric Lighting Model

Parametric models including Spherical Harmonics (SH) and Spherical Gaussians (SG) are commonly used for lighting representation. While second-order SH bases model the whole scene by only 9 coefficients for white illumination, and 27 coefficients for color illumination, and the simplified computation of rendering from SH coefficients as in [34], it is commonly adopted in differentiable pipelines such as [68]. However, Spherical Harmonics cannot represent high-frequency lighting sources such as point lights or small area lights. Spherical Gaussians, on the contrary, represent high-frequency lighting sources very well but have difficulties representing low-frequency lighting with limited parameters. It is natural to combine them as a hybrid representation of lighting HDR.

To fit Spherical Gaussians on a given HDR, we first identify the three brightest points in the HDR image and record their pixel coordinates. Subsequently, these coordinates are transformed into spherical coordinates as the center/mean of three SGs. To enforce SGs to fit small area lights, we fix the variance. The variance constitutes a diagonal matrix with all diagonal elements set to 0.005. Small SGs can fit high-frequency lighting for precise shadow rendering. Finally, we project the Spherical Gaussians onto the spherical panorama, and the difference between the lighting HDR and the lighting map of Spherical Gaussians is employed for fitting Spherical Harmonic lighting. We fit the second-order Spherical Harmonics for each channel, and there are 27 coefficients in total. SH lighting fits low-frequency lighting in the original HDR.

Examples of the hybrid representation of Spherical Harmonics and Spherical Gaussians are shown in Figure 15, by representing the original HDR as low-order Spherical Harmonics and several Spherical Gaussians, the rendered shading and shadows are similar to ground truths. We set the number of Spherical Gaussians as 3 in the pipeline. As shown in Figure 14, the renderings of the proposed pipeline are similar to the renderings of Blender. We can effectively render non-Lambertian surfaces, as well as precise cast shadows. The rendering step is detailed below. As lighting is addable, we can add the rendered images of SH and SGs to get the final rendering.

3.3.2 Non-Lambertian Rendering of Spherical Harmonics

Normal maps can be obtained from NeRFs by Eqn. 2 for a new view. We adopt the diffuse rendering layer according

to the Phong model, each ray ($\mathbf{r}$) corresponds to a pixel on the normal map:

$$I_d(\mathbf{r}) = \mathcal{R}(\mathbf{r})S(\mathbf{r}) = \mathcal{R}(\mathbf{r}) \sum_{\omega \in \mathcal{L}} l_\omega(L_\omega \cdot N(\mathbf{r})), \quad (7)$$

$\mathcal{R}(\mathbf{r})$ denotes the reflectance, and lighting can be replaced by SH representation as:

$$\mathcal{L} = \sum_{l=0}^{\infty} \sum_{m=-l}^{l} C_{l,m} Y_{l,m}, \quad (8)$$

$Y_{l,m}$ is the SH basis of degree l and order m, $C_{l,m}$ is the corresponding coefficient. Here we use up to the second order SH bases, i.e. $m \leq 2$, which are 9 bases in total.

We adopt the rendering process in [35], where Eqn. 7 becomes:

$$I_d(\mathbf{r}) = \mathcal{R}(\mathbf{r}) \sum_{\omega \in \mathcal{L}} l_\omega(L_\omega \cdot N(\mathbf{r})) = \mathcal{R}(\mathbf{r}) \sum_{l,m} \hat{A}_l C_{l,m} Y_{l,m}(\theta, \phi), \quad (9)$$

We also adopt the specular rendering layer from [65] to render the specular reflections by:

$$\begin{aligned} I_s(\mathbf{r}) &= s_p \sum_{\omega \in \mathcal{L}} l_\omega \left(\frac{L_\omega + v}{\|L_\omega + v\|} \cdot N(\mathbf{r}) \right)^\alpha \\ &\approx s_p \sum_{l,m} C_{l,m} (\hat{A}_l \hat{Y}_{l,m}(\theta, \phi))^\alpha. \end{aligned} \quad (10)$$

$\hat{Y}_{l,m}(\theta, \phi)$ are specular SH basis defined in [65]. s_p and α are material parameters controlling the specular reflectance and glossiness. By editing these parameters for each pixel, we can edit the material of each part of the composited scene. By adding I_d and I_s, we get the rendered image of Spherical Harmonic lighting.

3.3.3 Shading Rendering of Spherical Gaussians

We render each SG as 5 point lights, where the first point light is the SG center and others are sampled around the center with intensities diminishing according to Gaussian probabilities. Here if the lighting environment is a HDR, we can assume distant lighting, i.e. put SGs far from the scene. We can also model spatially variant lighting if the lights are put at 3D positions in the scene, with the light intensity diminishing as the distance of propagation increases. Shading k point lights with intensity $\mathbf{I}_i$ is rendered by:

$$\mathbf{S}_{SG}(\mathbf{r}) = \sum_{i=1}^{k} \frac{\mathbf{N}(\mathbf{r}) \cdot \mathbf{L}_i(\mathbf{r})}{|\mathbf{N}(\mathbf{r})||\mathbf{L}_i(\mathbf{r})|} * \frac{\mathbf{I}_i}{\gamma \cdot \mathbf{Dis}_i(\mathbf{r})^2}, \quad (11)$$

where $\mathbf{L}_i(\mathbf{r})$ is the ith new light's direction, which is calculated from the position of the light source to the target point.
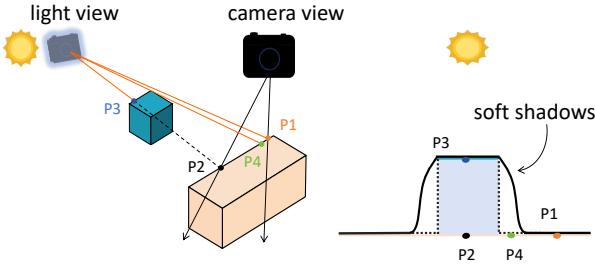
Figure 5. Variance shadow mapping. By comparing depth inconsistencies from the light view and the camera view, we have efficient shadow mapping for rendering cast shadows. For example, depths of P1 and P4 are consistent under two views, then they are visible. Depths of P2 are inconsistent in two views, so it is occluded, i.e. in shadows. In the right, blue areas are hard shadows by naive shadow mapping, where P4 is not in shadows. By variance shadow mapping, P4 is in soft shadows with visibility in $[0, 1]$.

If the lights are in the scene, i.e. they are spatially variant, then their directions vary from ray to ray. γ is a hyperparameter and $\mathbf{Dis}_i(\mathbf{r})$ is the distance between light and the 3D surface points corresponding to the ray $\mathbf{r}$. They are used to control the luminance of the light. Lights would decay as the distance to the light source gets larger, respecting the real lighting effects in the real world.

3.3.4 Shadow Rendering

The shadow effect is a crucial aspect of rendering, enhancing the realism of images by simulating the occlusion of light by objects. We use SGs to render cast shadows. We are inspired by the variance shadow-mapping ideas [14] from traditional computer graphics and propose a shadow rendering method fitting NeRFs. Specifically, according to the depth map and camera parameters, the coordinates of surface points in the 3D space can be obtained. We set a virtual camera at the light source and transform the depth map from the camera view to this new light view to obtain $z(\mathbf{r})$. We also render the square map of the depth, denoted as $\mathbf{X^2}$, and the depth map $\mathbf{X}$ directly from the light view. These two maps are subjected to box filtering, resulting in the filtered versions denoted as $\mu(\mathbf{X^2})$ and $\mu(\mathbf{X})$. Lastly, the probability of pixel $\mathbf{r}$ not being occluded, i.e. the visibility, can be expressed as:

$$\mathrm{V}(\mathbf{r}) = \begin{cases} 1, & z(\mathbf{r}) \leqslant \mu(\mathbf{X})(\mathbf{r_l}) \\ \frac{\sigma^2(\mathbf{r_l})}{\sigma^2(\mathbf{r_l}) + (z(\mathbf{r}) - \mu(\mathbf{X})(\mathbf{r_l}))^2}, & z(\mathbf{r}) > \mu(\mathbf{X})(\mathbf{r_l}) \end{cases} ,$$
$$\sigma^2(\mathbf{r_l}) = \mu(\mathbf{X^2})(\mathbf{r_l}) - \mu^2(\mathbf{X})(\mathbf{r_l})$$
$$(12)$$

where $\mathbf{r_l}$ is the correspondence pixel of $\mathbf{r}$ in light view. In Fig. 5, the left side illustrates the key insight of shadow mapping, which involves comparing the depths of the points to be rendered from the viewpoint of the light source. The right side demonstrates how variance shadow mapping transforms the discontinuous depth viewed from the perspective of the light source (represented by the black dashed line) into a continuous depth (illustrated by the black solid line), leading to a final shadow in a continuous range in $[0, 1]$.

This method only requires generating depth maps from two views, avoiding the cumulative transmittance of the light along the sampling point on the shadow ray. This approach works efficiently in practice. At last, we can get the final rendering for each ray $\mathbf{r}$ by:

$$I(\mathbf{r}) = I_d(\mathbf{r}) + I_s(\mathbf{r}) + V(\mathbf{r})\mathcal{R}(\mathbf{r})S_{SG}(\mathbf{r}). \qquad (13)$$

4. Experiments

We conduct experiments for intrinsic decomposition, ablations, and relighting.

4.1. Implementation Details

We adopt the codes of MipNeRF360 [4] as the NeRF backbone and implement the method within the JAX framework [10]. Our model was trained on an RTX 3080 Ti GPU using the Adam optimizer [20] for a total of 100 thousand iterations. Throughout the training process, one image was randomly sampled from the input images per iteration, with a batch size set to 1024. To facilitate the acquisition of neighboring pixels $\mathbf{r}_{adj}$ and non-neighbor pixels $\mathbf{r}'$, we adopt distance-aware sampling from [62]. In all experiments, we set parameters as $\lambda_0 = 1$, $\lambda_1 = 0.01$, $\lambda_2 = 0.1$, $\lambda_3 = 1$, $\lambda_4 = 0.01$, $\lambda_5 = 0.005$, $\lambda_6 = 0.1$, $\lambda_7 = 0.001$. The evaluations leverage MipNeRF360 datasets [4], Blender datasets [30], and Invrender datasets [74]. The evaluation metrics include Peak Signal-to-Noise Ratio (PSNR), Mean Squared Error (MSE), Structural Similarity Index Measure (SSIM) [49] and Learned Perceptual Image Patch Similarity (LPIPS) [72].

4.2. Comparsions

4.2.1 Intrinsic Decomposition

Although the proposed method decomposes intrinsic NeRFs, we also compare them with intrinsic image decomposition baselines, which take a single image as input. We compare with USI3D [28] and SIRFS [3], which solve the intrinsic image decomposition from a single picture. We also compare with Invrender [74], Ref-NeRF [47] and IntrinsicNeRF [62], which combine NeRF with inverse rendering decomposition, taking multi-view images as inputs. Specifically, we use the dataset from Invrender [74] and evaluate the decomposed reflectance. Fig. 6 shows the reflectance images decomposed by our method and five other
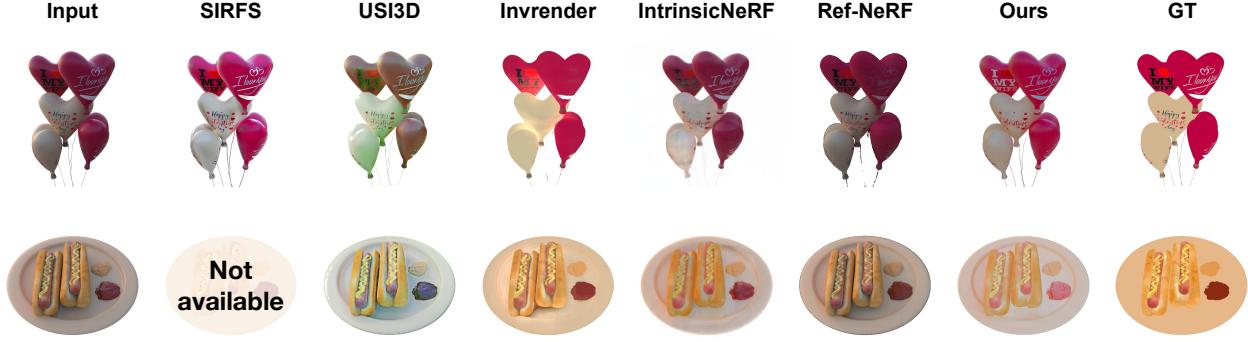
Figure 6. Reflectance decomposition results. SIRFS [3] and USI3D [28] are tested directly using pre-trained networks.Invrender [74], IntrinsicNeRF [62], Ref-NeRF [47], and our method use the same training data.

Figure 7. New perspective synthesis results for objects. Our method achieves superior results in novel view synthesis compared to Invrender.

methods. Table 1 presents the quantitative evaluation results. The decomposition results based on a single image are not satisfactory due to the lack of information from multiple perspective images. They cannot decompose correct reflectance colors due to ambiguities. Methods from multi-view input can fully utilize cross-view information and successfully decompose better reflectance colors. SIRFS [3] fails to decompose in hotdog data. Invrender [74] achieves the best performance on error metrics, but their reflectance loses many details, such as the texts on the balloons in Fig. 7. They also have difficulties in predicting objects with complicated geometry. IntrinsicNeRF [62] get comparable results with us by extra semantic information. Ref-NeRF [47] fails to effectively separate the reflectance and geometry information, particularly for objects with Lambertian surfaces.

	MSE↓	PSNR↑	SSIM↑	LPIPS↓
USI3D	0.0097	21.8434	0.9263	0.1395
SIRFS	0.0089	20.6065	0.9294	0.1097
Invrender	**0.0019**	**28.1937**	**0.9336**	**0.0764**
IntrinsicNeRF	0.0038	25.1896	0.9221	0.0871
Ref-NeRF	0.0042	24.5182	0.9186	0.0985
Ours	0.0037	25.6568	0.9314	0.0784

Table 1. Quantitative evaluations of decomposed reflectance. The best values are in bold, and the second-best values are underlined.

	MSE↓	PSNR↑	SSIM↑	LPIPS↓
Invrender	0.0011	29.7887	0.9461	0.0809
Ours	**0.0004**	**34.9118**	**0.9675**	**0.0346**

Table 2. Quantitative evaluations for novel view synthesis.

4.2.2 Novel View Synthesis

For novel view synthesis, we compare our results with Invrender [62]. The results are shown in Fig. 7. As we can see in Fig. 7, the images rendered by Invrender lose the original details of the object, such as the text on the balloon and the round metal screws on the back of the chair. They cannot handle objects with small or complex textures very well. Our method surpasses Invrender across all metrics, with the results presented in Table 2.

4.2.3 Normal Reconstruction

The normal estimation of our method is based on the NeRF backbone. We compare our method with Ref-NeRF [47], another NeRF-based method. The dataset of Invrender was reconstructed on Ref-NeRF and our method. The left part of Fig. 8 shows the reconstruction results of Ref-NeRF. It is observed that the surface reconstructed by our method is smoother such as the back of the chair and the surface of the balloon. This is because we adopt the constraint of normal smoothing and restrict the consistency between normal and shading, resulting in a reasonable physical connection between geometry and lighting.

4.3. Scene Composition and Relighting

For composition, we use the MipNeRF360 dataset [4] as scene data, the Blender dataset [30], and the Invrender dataset [74] as object data. We use four different scene and object pairs in experiments. In Fig. 9, The input scene and object pairs are shown on the left, and relightings by three different lighting conditions from different views are shown on the right.
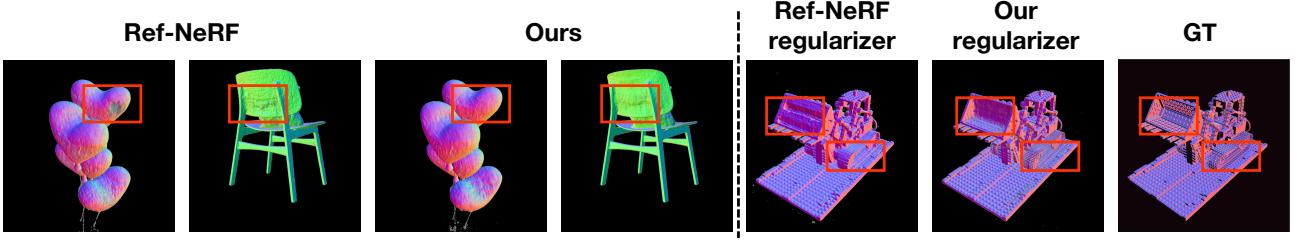
Figure 8. Normal comparisons with Ref-NeRF. The left part shows the normal reconstruction results of Ref-NeRF and our method. The right part compares the normal reconstruction with the regularizer of Ref-NeRF and ours.
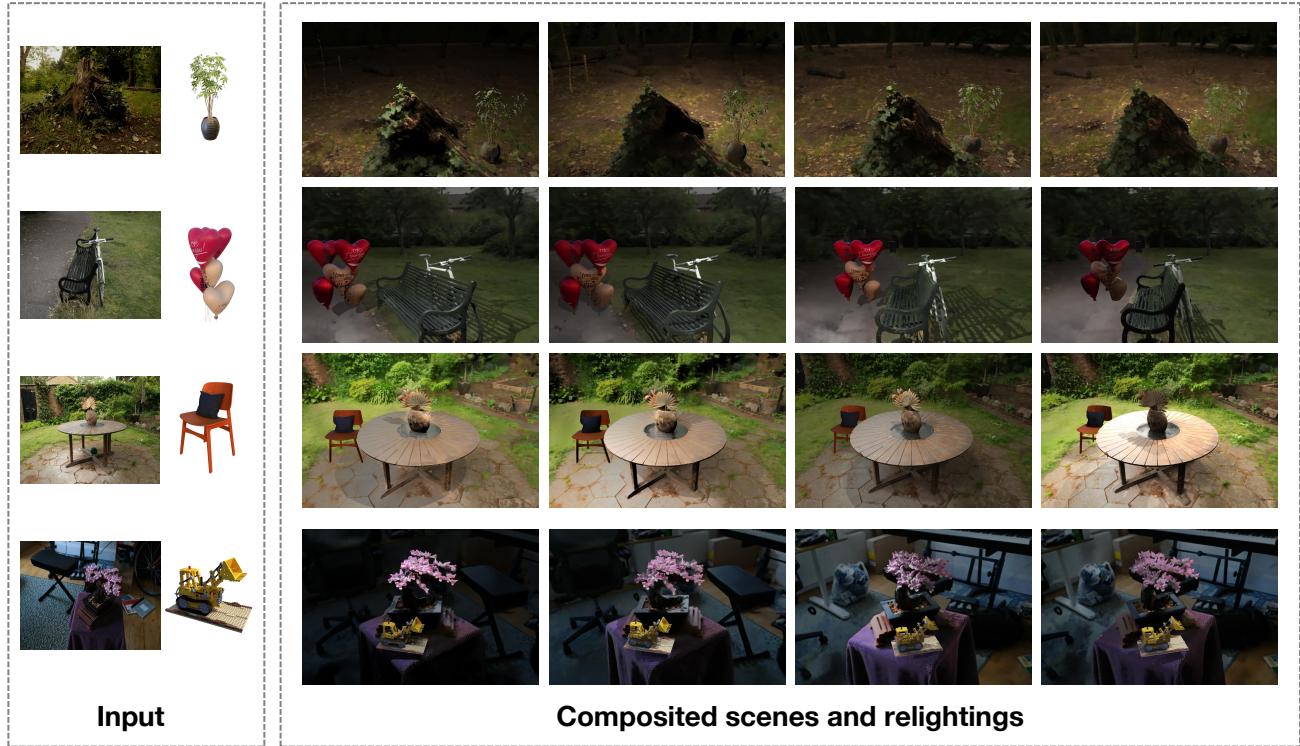

Input

Composited scenes and relightings

Figure 9. Composition and relighting results of four scene-object pairs. For each composited scene, we relight them under 4 different lighting.
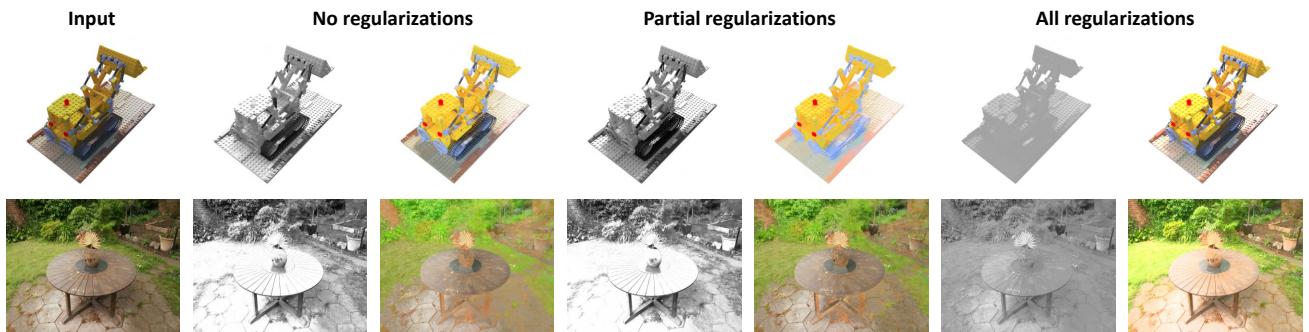

Input **No regularizations** **Partial regularizations** **All regularizations**

Figure 10. Ablation studies on regularization constraints. "No regularizations" denotes trained with only RGB loss. "Partial regularizations" denotes constraints of IntrinsicNeRF [62] ($\mathcal{L}_{chro}$, $\mathcal{L}_{rs}$, $\mathcal{L}_{rns}$).
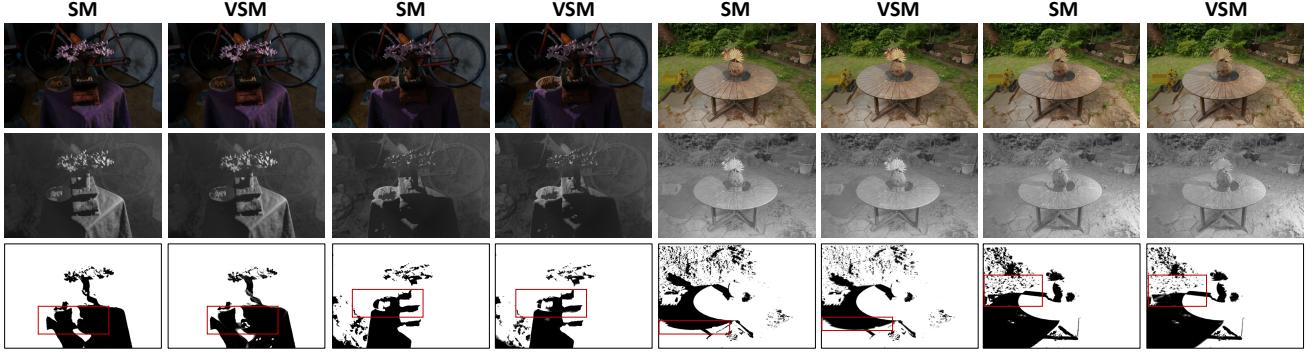
Figure 11. Comparisons between variance shadow mapping (VSM) and naive shadow mapping (SM). The odd and even columns are paired for comparison. From top to bottom, three rows are rendered images, SG shadings, and cast shadows. VSM can model soft shadows while SM models only hard shadows.

Figure 12. Relighting with nearby (left) and faraway (right) SG lighting, producing soft shadows (left) or sparse shadows (right).

Through efficient shadow addition, we have achieved the effect of scene and object interaction of casting shadows on each other. For example, in the last column, the shadow of the plant is cast onto the Lego. The proposed method supports relighting from arbitrary views. Previous methods of single-image object insertions can only relight the single-view image.

4.4. Ablations

To verify the effectiveness of our method, we conducted several ablation studies. The scene data is sourced from MipNeRF360 [4], and the object data is from NeRF [30]. Ablations of "decomposition with and without regularization constraints", "variance shadow mapping and naive shadow mapping", "shading replacement" and "hybrid parametric lighting model" are introduced below.

4.4.1 Regularization Loss

Since the unsupervised intrinsic image decomposition problem is ill-posed, we add some regularization constraints. We conduct ablation studies on these regularization losses. We test three settings, without adding any regularization losses, using partial regularization losses ($\mathcal{L}_{chro}$, $\mathcal{L}_{rs}$, $\mathcal{L}_{rns}$), and using all regularization losses. Fig. 10 shows the comparison results of the three settings. Without any regularization constraints, reflectance and shading decomposition are

relatively arbitrary. Both are not very accurate. After using some regularization from IntrinsicNeRF [62], the reflectance becomes more flattened, but the shading is unsatisfactory. The shading contains too much color information belonging to reflectance. With all regularization constraints, it decomposes the shading image much better, not including surface colors. The decoupling effect of shading results in a better and more accurate representation of the lighting conditions. For example, in the case of the Lego wheel, the shading generated by our method does not include the color of the wheel. Instead, the black color of the wheel, derived from partial regularization, is still black in the shading.

Considering that the Ref-NeRF [47] also adopts normal regularization, we replace our normal regularizer with the Ref-NeRF regularizer in our method. The result of the comparison between the two regularizers is shown in the right part of Fig. 8. Qualitatively, the geometry by Ref-NeRF regularizer is over-smoothed in small structures, such as the wheels and shovel of Lego (in the red box in Fig. 8).

4.4.2 Variance Shadow Mapping vs Naive Shadow Mapping

We compare naive shadow mapping with variance shadow mapping to demonstrate the soft shadows. In naive shadow mapping, due to the lack of handling abrupt changes in depth in regular shadow mapping, the resulting shadows are
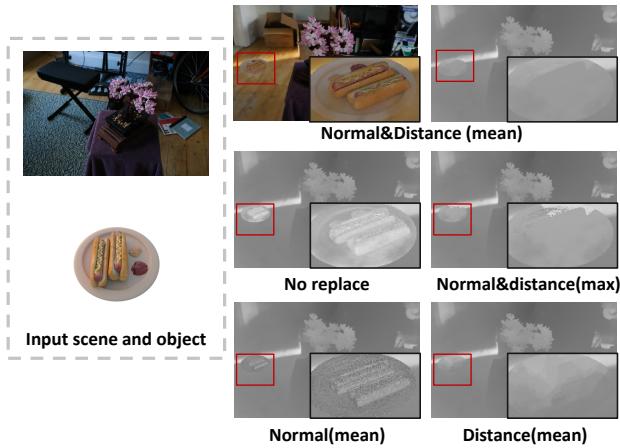
Figure 13. Ablation experiments on shading replacement. At the left side, the first row shows the shadow replacing strategy adopted in the method, and the last two rows show other alternatives.

Figure 14. Relighting by the proposed renderer and Blender.

discrete values of 0 and 1 and the shadow edges are abrupt and sharp. It can only produce hard shadows. Variance shadow mapping smoothens the depth and calculates the probability of shadows using Chebyshev's inequality, leading to smoother shadow edges. As illustrated in Fig. 11, at the edges of the shadows, like the shadow edge of a table on the ground in a garden scene or the shadow edge of a plate in a bonsai scene, there is a gradient effect, creating a soft shadow effect. Additionally, variance shadow mapping requires storing two depth maps and filtering them, resulting in only slightly increased computational overhead compared to shadow mapping. Therefore, we select variance shadow mapping as the method for shadow generation. When the SGs are near from each other, it generate soft shadows as in Fig. 12 (left). When SGs are far from each other as in Fig. 12 (right), the shadows are also sparsely distributed, similar in the real cases.

4.4.3 Shading Replacement

Due to substantial lighting variations, relighting objects after insertion into a scene becomes crucial. This relighting is achieved through shading replacement, avoiding the need to infer scene illumination. By specifying a confidence level p, the top p pairs are selected based on a scoring system considering factors such as normal similarity, distance score, and their product. Solely relying on normal similarity results in global shading, while focusing solely on distance fails to align with physical interpretations. However, by combining both factors, it becomes feasible to attain query shading within a localized range. On the other hand, we compare two strategies, taking the average and maximum shading of p points. As in Fig. 13, directly inserting a hot dog into the scene leads to an unrealistic composition, as
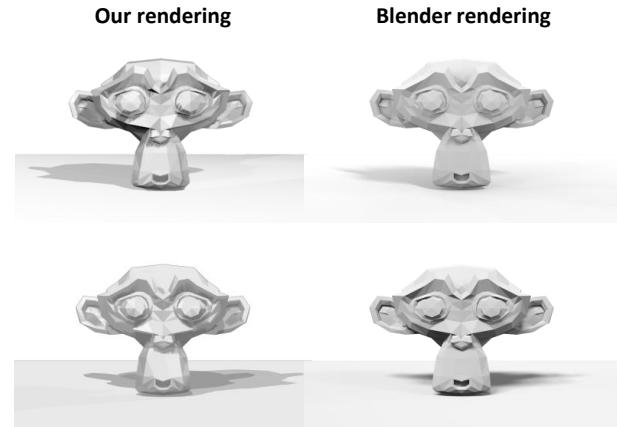
the original lighting environment of the hot dog is different from the scene lighting. When we replace the shading of the hot dog, the composition of the hot dog and the scene are more consistent. Replacing shading with normal similarity results in too much noise. Replacing shading with maximum values cannot generate plausible shading. Using mean shading gives a reasonable result without introducing noises.

4.4.4 Hybrid Parametric Lighting Model

we conduct ablation experiments on the hybrid parametric lighting model and the standalone SH lighting model, as well as ablation experiments with different numbers of SG. Specifically, we render the original HDR, SH representation and SH+SG representation in Blender, to compare the accuracy of the hybrid lighting representation. As in Fig. 15, Spherical Harmonics (SH) is capable of fitting only low-frequency lighting, and the resulting renderings lack distinct shadows. Our hybrid model was able to produce noticeable shadows, showcasing its ability to capture both low- and high-frequency lighting in original HDRs. Additionally, we found that increasing the number of SGs can bring the results closer to ground truth (HDR), while the computational costs also increase. We observe that when the number of SGs reached 3, the experimental outcomes are already sufficiently representative of the real scenario, even for indoor scenes. Outdoor scenes are even simpler with one dominant lighting source (sun or moon). Further increasing the number of SGs does not significantly alter the results. So we set the number of SGs as 3 in all relighting experiments.

We also compare the rendering of our pipeline with Blender in Figure 14. While our renderer is much more efficient, the rendered images and shadows are similar, while Blender still generates more soft shadow edges.
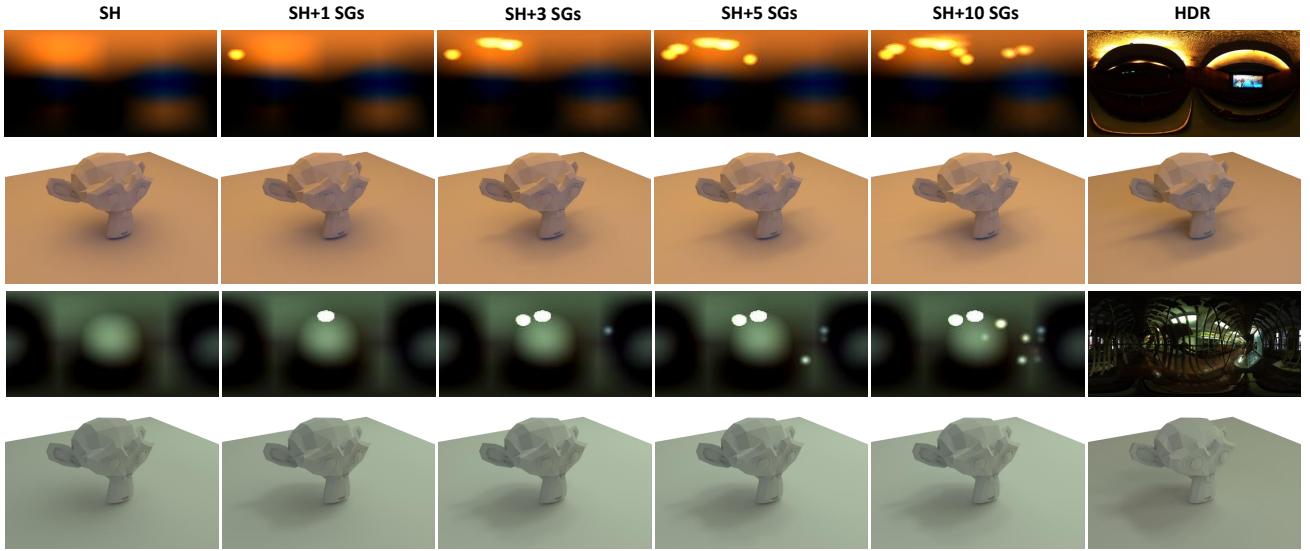
Figure 15. Hybrid parametric lighting model. The render results of the SH lighting model, hybrid parametric lighting model, and GT. The first and third rows are spherical lighting maps. The second and fourth rows are corresponding renderings.

Figure 16. Demonstration of the re-colorization effects. The reflectance of the original objects are changed after intrinsic decomposition.

4.5. Application

The proposed method has many applications, except for scene composition and relighting. Here we show the effect of changing the color of objects by modifying their reflectance in NeRFs. As shown in Fig. 16, we insert 2 different chairs into the room scene and modify them to different colors. In the first row, purple Lego and blue balloons are inserted into the bike scene. In Fig. 17, we change the material of the pillow, table, and vase of the original scene by making them more specular. Compared to the all-diffuse scene, we can edit the material of each part of the composited scene.
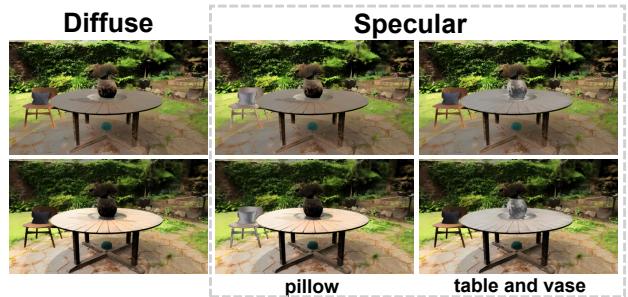

Figure 17. Demonstration of re-material effects. The first row shows all-diffuse results, while the subsequent rows demonstrate re-material results of pillows and vases respectively.

5. Conclusions

We propose a method for compositing objects and scenes in NeRFs. The object insertion considers the lighting consistency in the composited scene, or relighting the whole scene. We use a hybrid representation of Spherical Harmonics and Spherical Gaussians, to support non-Lambertian rendering with shadows. One limitation is manually setting an insertion position instead of automatically attaching to surfaces. Ideally, automatically attached to nearby surfaces would be more practical in AR applications. We will further explore such physical interactions.

References

[1] Thomas Annen, Tom Mertens, Philippe Bekaert, Hans-Peter Seidel, and Jan Kautz. Convolution shadow maps. In *Proceedings of the 18th Eurographics Conference on Rendering*

Techniques, EGSR'07, page 51–60, Goslar, DEU, 2007. Eurographics Association. 3

[2] Yacov Hel-Or Asaf Karnieli, Ohad Fried. Deepshadow: Neural shape from shadows. In *ECCV*, 2022. 3

[3] J. T. Barron and J. Malik. Shape, illumination, and reflectance from shading. IEEE Transactions on Pattern Analysis and Machine Intelligence, 37(8):1670–1687, 2015. 7, 8

[4] J. T. Barron, B. Mildenhall, D. Verbin, P. P. Srinivasan, and P. Hedman. Mip-nerf 360: Unbounded anti-aliased neural radiance fields. *arXiv e-prints*, 2021. 2, 7, 8, 10

[5] Jonathan T. Barron, Ben Mildenhall, Matthew Tancik, Peter Hedman, Ricardo Martin-Brualla, and Pratul P. Srinivasan. Mip-nerf: A multiscale representation for anti-aliasing neural radiance fields, 2021.

[6] S. Bi, Z. Xu, P. Srinivasan, B. Mildenhall, and R. Ramamoorthi. Neural reflectance fields for appearance acquisition, 2020. 2

[7] M. Boss, R. Braun, V. Jampani, J. T. Barron, and Hpa Lensch. Nerd: Neural reflectance decomposition from image collections. 2020. 2

[8] M. Boss, V. Jampani, R. Braun, C. Liu, J. T. Barron, and Hpa Lensch. Neural-pil: Neural pre-integrated lighting for reflectance decomposition. 2021. 2

[9] Mark Boss, Andreas Engelhardt, Abhishek Kar, Yuanzhen Li, Deqing Sun, Jonathan T. Barron, Hendrik P.A. Lensch, and Varun Jampani. SAMURAI: Shape And Material from Unconstrained Real-world Arbitrary Image collections. In *Advances in Neural Information Processing Systems (NeurIPS)*, 2022. 2

[10] James Bradbury, Roy Frostig, Peter Hawkins, Matthew James Johnson, Chris Leary, Dougal Maclaurin, George Necula, Adam Paszke, Jake VanderPlas, Skye Wanderman-Milne, and Qiao Zhang. JAX: composable transformations of Python+NumPy programs, 2018. 7

[11] R Martin Brualla, K. Park, U. Sinha, S. Bouaziz, D. Goldman, J. T. Barron, and S. M. Seitz. Deformable neural radiance fields, 2022. 2

[12] Changwoon Choi, Juhyeon Kim, and Young Min Kim. Iblnerf: Image-based lighting formulation of neural radiance fields, 2023. 2

[13] Maximilian Denninger, Martin Sundermeyer, Dominik Winkelbauer, Dmitry Olefir, Tomas Hodan, Youssef Zidan, Mohamad Elbadrawy, Markus Knauer, Harinandan Katam, and Ahsan Lodhi. Blenderproc: Reducing the reality gap with photorealistic rendering. In *International Conference on Robotics: Sciene and Systems, RSS 2020*, 2020.

[14] William Donnelly and Andrew Lauritzen. Variance shadow maps. In *ACM Symposium on Interactive 3D Graphics and Games*, 2006. 3, 7

[15] Randima Fernando. Percentage-closer soft shadows. In *International Conference on Computer Graphics and Interactive Techniques*, 2005. 3

[16] Sara Fridovich-Keil, Alex Yu, Matthew Tancik, Qinhong Chen, Benjamin Recht, and Angjoo Kanazawa. Plenoxels: Radiance fields without neural networks. In *Proceedings of the IEEE/CVF Conference on Computer Vision and Pattern Recognition*, pages 5501–5510, 2022.

[17] Jiatao Gu, Lingjie Liu, Peng Wang, and Christian Theobalt. Stylenerf: A style-based 3d-aware generator for high-resolution image synthesis, 2021.

[18] M. Guo, A. Fathi, J. Wu, and T. Funkhouser. Object-centric neural scene rendering. 2020. 3

[19] Meghna Asthana;William Smith;Patrik Huber. Neural apparent brdf fields for multiview photometric stereo. In *CVMP '22: Proceedings of the 19th ACM SIGGRAPH European Conference on Visual Media Production*, 2022. 2

[20] Diederik P Kingma and Jimmy Ba. Adam: A method for stochastic optimization. *arXiv: Learning*, 2014. 7

[21] Sosuke Kobayashi, Eiichi Matsumoto, and Vincent Sitzmann. Decomposing nerf for editing via feature field distillation, 2022. 3

[22] V. Lazova, V. Guzov, K. Olszewski, S. Tulyakov, and G. Pons-Moll. Control-nerf: Editable feature volumes for scene rendering and manipulation. 2022. 3

[23] Noah Li, Zhengqi;Snavely. Cgintrinsics: Better intrinsic image decomposition through physically-based rendering. *Computer Vision and Pattern Recognition*, pages 381–399, 2018. 2

[24] C. H. Lin, W. C. Ma, A. Torralba, and S. Lucey. Barf: Bundle-adjusting neural radiance fields, 2021. 2

[25] Y. C. Lin, P. Florence, J. T. Barron, A. Rodriguez, and T. Y. Lin. inerf: Inverting neural radiance fields for pose estimation. 2020.

[26] L. Liu, J. Gu, K. Z. Lin, T. S. Chua, and C. Theobalt. Neural sparse voxel fields. 2020.

[27] Steven Liu, Xiuming Zhang, Zhoutong Zhang, Richard Zhang, Jun-Yan Zhu, and Bryan Russell. Editing conditional radiance fields, 2021.

[28] Yunfei Liu, Yu Li, Shaodi You, and Feng Lu. Unsupervised learning for intrinsic image decomposition from a single image. In *CVPR*, 2020. 7, 8

[29] Linjie Lyu, Ayush Tewari, Thomas Leimkuehler, Marc Habermann, and Christian Theobalt. Neural radiance transfer fields for relightable novel-view synthesis with global illumination. In *ECCV*, 2022. 2

[30] B. Mildenhall, P. P. Srinivasan, M. Tancik, J. T. Barron, R. Ramamoorthi, and N. Ren. Nerf: Representing scenes as neural radiance fields for view synthesis. 2020. 1, 2, 7, 8, 10

[31] Michael Niemeyer and Andreas Geiger. GIRAFFE: Representing scenes as compositional generative neural feature fields. *https://arxiv.org/abs/2011.12100*, 2020. 2

[32] Christoph Peters and Reinhard Klein. Moment shadow mapping. In *Proceedings of the 19th Symposium on Interactive 3D Graphics and Games*, i3D '15, page 7–14, New York, NY, USA, 2015. Association for Computing Machinery. 3

[33] A. Pumarola, E. Corona, G. Pons-Moll, and F. Moreno-Noguer. D-nerf: Neural radiance fields for dynamic scenes. 2020.

[34] Ravi Ramamoorthi and Pat Hanrahan. An efficient representation for irradiance environment maps. In *Proceedings of the 28th annual conference on Computer graphics and interactive techniques*, pages 497–500, 2001. 6

[35] Ravi Ramamoorthi and Pat Hanrahan. On the relationship between radiance and irradiance: determining the illumination from images of a convex lambertian object. *JOSA A*, 18(10):2448–2459, 2001. 6

[36] D. Rebain, W. Jiang, S. Yazdani, K. Li, K. M. Yi, and A. Tagliasacchi. Derf: Decomposed radiance fields. 2020. 2

[37] William T. Reeves, David H. Salesin, and Robert L. Cook. Rendering antialiased shadows with depth maps. *SIGGRAPH Comput. Graph.*, 21(4):283–291, aug 1987. 3

[38] C. Reiser, S. Peng, Y. Liao, and A. Geiger. Kilonerf: Speeding up neural radiance fields with thousands of tiny mlps. 2021.

[39] Viktor Rudnev, Mohamed Elgharib, William Smith, Lingjie Liu, Vladislav Golyanik, and Christian Theobalt. Neural radiance fields for outdoor scene relighting. 2021. 2

[40] Katja Schwarz, Yiyi Liao, Michael Niemeyer, and Andreas Geiger. Graf: Generative radiance fields for 3D-aware image synthesis. In *Advances in Neural Information Processing Systems (NeurIPS)*, volume 33, 2020.

[41] M. L. Shih, S. Y. Su, J. Kopf, and J. B. Huang. 3d photography using context-aware layered depth inpainting. *IEEE*, 2020.

[42] P. P. Srinivasan, B. Deng, X. Zhang, M. Tancik, B. Mildenhall, and J. T. Barron. Nerv: Neural reflectance and visibility fields for relighting and view synthesis. In *Computer Vision and Pattern Recognition*, 2021. 2

[43] C. Sun, M. Sun, and H. T. Chen. Direct voxel grid optimization: Super-fast convergence for radiance fields reconstruction. 2021.

[44] Jiaxiang Tang, Xiaokang Chen, Jingbo Wang, and Gang Zeng. Compressible-composable nerf via rank-residual decomposition, 2022. 3

[45] Kushagra Tiwary, Tzofi Klinghoffer, and Ramesh Raskar. Towards learning neural representations from shadows. In *Computer Vision – ECCV 2022: 17th European Conference, Tel Aviv, Israel, October 23–27, 2022, Proceedings, Part XXXIII*, page 300–316, Berlin, Heidelberg, 2022. Springer-Verlag. 3

[46] Marco Toschi, Riccardo De Matteo, Riccardo Spezialetti, Daniele De Gregorio, Luigi Di Stefano, and Samuele Salti. Relight my nerf: A dataset for novel view synthesis and relighting of real world objects. In *2023 IEEE/CVF Conference on Computer Vision and Pattern Recognition (CVPR)*.

[47] Dor Verbin, Peter Hedman, Ben Mildenhall, Todd Zickler, Jonathan T Barron, and Pratul P Srinivasan. Ref-nerf: Structured view-dependent appearance for neural radiance fields.

In *2022 IEEE/CVF Conference on Computer Vision and Pattern Recognition (CVPR)*, pages 5481–5490. IEEE, 2022. 7, 8, 10

[48] Yuxin Wang, Wayne Wu, and Dan Xu. Learning unified decompositional and compositional nerf for editable novel view synthesis. In *ICCV*, 2023. 3

[49] Z. Wang, W. Pan, N. Cuppens-Boulahia, F. Cuppens, and C. Roux. Image quality assessment: From error visibility to structural similarity. 2013. 7

[50] Z. Wang, S. Wu, W. Xie, M. Chen, and V. A. Prisacariu. Nerf−−: Neural radiance fields without known camera parameters. 2021.

[51] Zian Wang, Tianchang Shen, Jun Gao, Shengyu Huang, Jacob Munkberg, Jon Hasselgren, Zan Gojcic, Wenzheng Chen, and Sanja Fidler. Neural fields meet explicit geometric representation for inverse rendering of urban scenes, 2023. 3

[52] O. Wiles, G. Gkioxari, R. Szeliski, and J. Johnson. Synsin: End-to-end view synthesis from a single image. In *2020 IEEE/CVF Conference on Computer Vision and Pattern Recognition (CVPR)*, 2020.

[53] L. Williams. Casting curved shadows on curved surfaces. In *ACM*, 1978.

[54] Lance Williams. Casting curved shadows on curved surfaces. In *Proceedings of the 5th Annual Conference on Computer Graphics and Interactive Techniques*, SIGGRAPH '78, page 270–274, New York, NY, USA, 1978. Association for Computing Machinery.

[55] Lance Williams. Casting curved shadows on curved surfaces. *SIGGRAPH Comput. Graph.*, 12(3):270–274, aug 1978. 3

[56] Lance Williams. *Casting curved shadows on curved surfaces*, page 51–55. Association for Computing Machinery, New York, NY, USA, 1998.

[57] Qianyi Wu, Xian Liu, Yuedong Chen, Kejie Li, Chuanxia Zheng, Jianfei Cai, and Jianmin Zheng. Object-compositional neural implicit surfaces. In *European Conference on Computer Vision*, 2022. 3

[58] Qianyi Wu, Kaisiyuan Wang, Kejie Li, Jianmin Zheng, and Jianfei Cai. Objectsdf++: Improved object-compositional neural implicit surfaces. In *Proceedings of the IEEE/CVF International Conference on Computer Vision*, 2023. 3

[59] Bangbang Yang, Yinda Zhang, Yinghao Xu, Yijin Li, Han Zhou, Hujun Bao, Guofeng Zhang, and Zhaopeng Cui. Learning object-compositional neural radiance field for editable scene rendering. In *International Conference on Computer Vision (ICCV)*, October 2021. 3

[60] Yao Yao, Jingyang Zhang, Jingbo Liu, Yihang Qu, Tian Fang, David Mckinnon, Yanghai Tsin, and Long Quan. Neilf: Neural incident light field for physically-based material estimation. 2022. 2

[61] Lior Yariv, Yoni Kasten, Dror Moran, Meirav Galun, Matan Atzmon, Basri Ronen, and Yaron Lipman. Multiview neural surface reconstruction by disentangling geometry and appearance. *Advances in Neural Information Processing Systems*, 33:2492–2502, 2020.

[62] Weicai Ye, Shuo Chen, Chong Bao, Hujun Bao, Marc Polle-feys, Zhaopeng Cui, and Guofeng Zhang. Intrinsicnerf: Learning intrinsic neural radiance fields for editable novel view synthesis, 2023. 3, 7, 8, 9, 10

[63] Yunfan Ye, Renjiao Yi, Zhirui Gao, Chenyang Zhu, Zhiping Cai, and Kai Xu. Nef: Neural edge fields for 3d parametric curve reconstruction from multi-view images. In *Proceedings of the IEEE/CVF Conference on Computer Vision and Pattern Recognition (CVPR)*, pages 8486–8495, June 2023. 2

[64] Renjiao Yi, Chenyang Zhu, Ping Tan, and Stephen Lin. Faces as lighting probes via unsupervised deep highlight extrac-tion. In *Proceedings of the European Conference on com-puter vision (ECCV)*, pages 317–333, 2018. 2

[65] Renjiao Yi, Chenyang Zhu, and Kai Xu. Weakly-supervised single-view image relighting. In *Proceedings of the IEEE/CVF Conference on Computer Vision and Pattern Recognition*, pages 8402–8411, 2023. 2, 6

[66] Hong-Xing Yu, Samir Agarwala, Charles Herrmann, Richard Szeliski, Noah Snavely, Jiajun Wu, and Deqing Sun. Accidental light probes. In *Proceedings of the IEEE/CVF Conference on Computer Vision and Pattern Recognition*, pages 12521–12530, 2023. 2

[67] Hong-Xing Yu, Michelle Guo, Alireza Fathi, Yen-Yu Chang, Eric Ryan Chan, Ruohan Gao, Thomas Funkhouser, and Ji-ajun Wu. Learning object-centric neural scattering functions for free-viewpoint relighting and scene composition. *Trans-actions on Machine Learning Research*, 2023.

[68] Ye Yu and William AP Smith. Inverserendernet: Learn-ing single image inverse rendering. In *Proceedings of the IEEE/CVF Conference on Computer Vision and Pattern Recognition*, pages 3155–3164, 2019. 6

[69] Chong Zeng, Guojun Chen, Yue Dong, Pieter Peers, Hongzhi Wu, and Xin Tong. Relighting neural radiance fields with shadow and highlight hints. In *ACM SIGGRAPH 2023 Con-ference Proceedings*, 2023. 2

[70] Jingyang Zhang, Yao Yao, Shiwei Li, Jingbo Liu, Tian Fang, David McKinnon, Yanghai Tsin, and Long Quan. Neilf++: Inter-reflectable light fields for geometry and material esti-mation. 2

[71] Kai Zhang, Fujun Luan, Qianqian Wang, Kavita Bala, and Noah Snavely. Physg: Inverse rendering with spherical gaus-sians for physics-based material editing and relighting. 2021. 2

[72] Richard Zhang, Phillip Isola, Alexei A Efros, Eli Shechtman, and Oliver Wang. The unreasonable effectiveness of deep features as a perceptual metric. In *CVPR*, 2018. 7

[73] X. Zhang, P. P. Srinivasan, B. Deng, P. Debevec, W. T. Free-man, and J. T. Barron. Nerfactor: Neural factorization of shape and reflectance under an unknown illumination. 2021. 2

[74] Yuanqing Zhang, Jiaming Sun, Xingyi He, Huan Fu, Rongfei Jia, and Xiaowei Zhou. Modeling indirect illumination for inverse rendering. In *CVPR*, 2022. 7, 8

[75] T. Zhou, R. Tucker, J. Flynn, G. Fyffe, and N. Snavely. Stereo magnification: Learning view synthesis using mul-tiplane images. *ACM Transactions on Graphics*, 37(4):1–12, 2018.